Supplementary Information for

Rapid fabrication of reconfigurable helical microswimmers with environmentally adaptive locomotion

Rui Li[1, ‡], Yuan Tao[1, ‡], Jiawen Li[1, *], Dongdong Jin[2], Chen Xin[1], Shengyun Ji[1], Chaowei Wang[1], Yachao Zhang[1], Yanlei Hu[1], Dong Wu[1], Li Zhang[2, *], and Jiaru Chu[1]

[1] CAS Key Laboratory of Mechanical Behavior and Design of Materials, Department of Precision Machinery and Precision Instrumentation, University of Science and Technology of China, Hefei 230026, China.

[2] Department of Mechanical and Automation Engineering, The Chinese University of Hong Kong, Hong Kong 999077, China.

* jwl@ustc.edu.cn

*lizhang@mae.cuhk.edu.hk

‡ These authors contributed equally to this paper.

This PDF files includes:

Supplementary Figures:

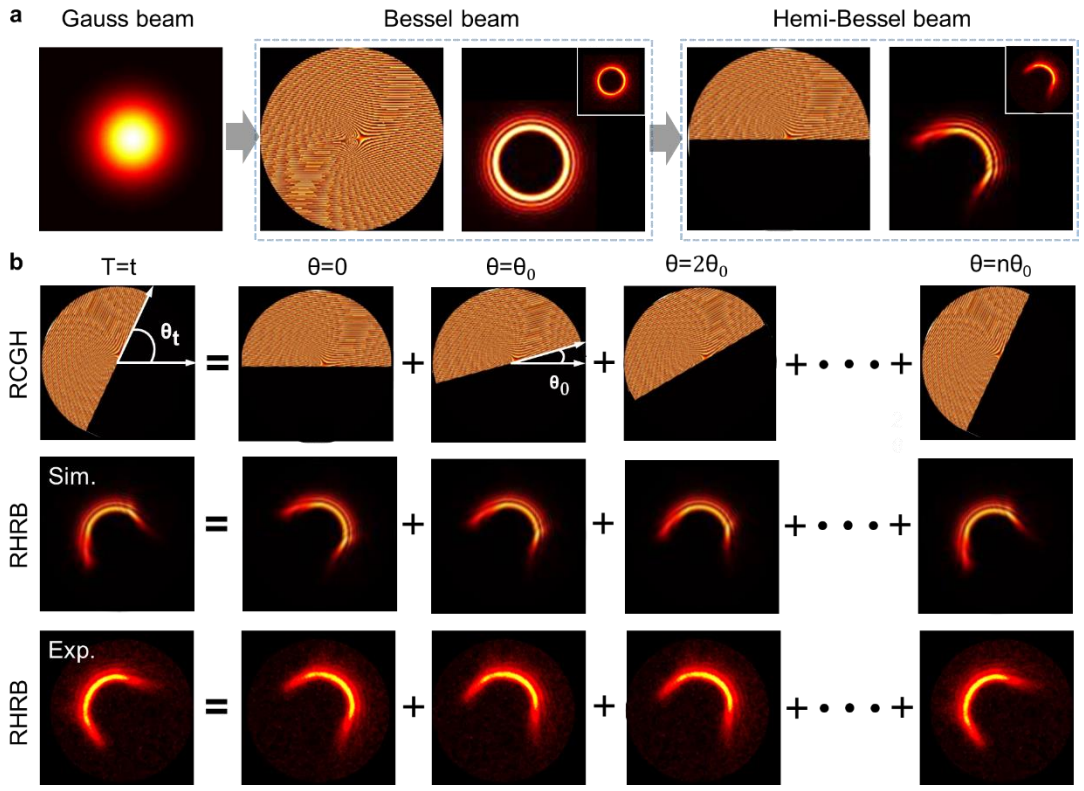

Figure S1. The generation process of RHRB. (a) The holographic modulation of light beam (simulation results) from Gauss Beam to Bessel beam and to hemi-Bessel beam. The insets show the experimental results. (b) The generation of RHRH and RHRB (simulation and experimental results)). The RCGH is a GIF animation generated by superimposing different CGHs with equally increased oblique angle in time sequence. The oblique angle is θ_t at time t. Correspondingly, the RHRB is a rotating light field. There is a one-to-one correlation between the RCGH and the RHRB. Therefore, the rotating angle θ_0 can not only denotes the angular difference between adjacent CGHs of RCGH, but also denotes the angular difference of RHRB.

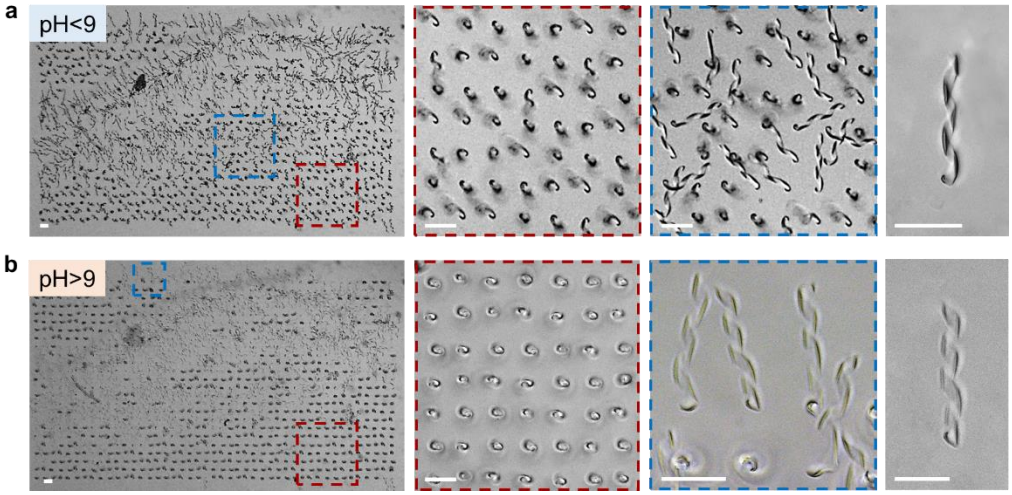

Figure S2. The large array of one thousand microhelices fabricated by the rotary holographic processing strategy within half an hour in contracted state (a) and expanded state (b). The microhelices are too soft and too high, and some have fallen down. Scale bar: 50 μm.

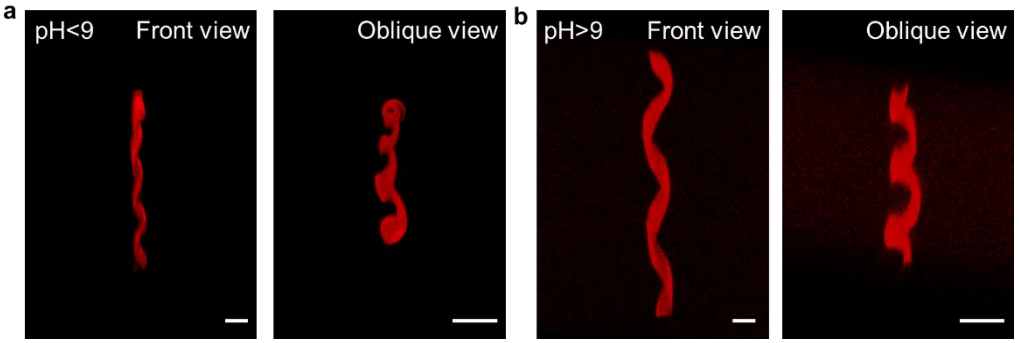

Figure S3. The laser confocal microscopy of microhelices before swelling (a) and after swelling (b). Scale bar: 10 μm

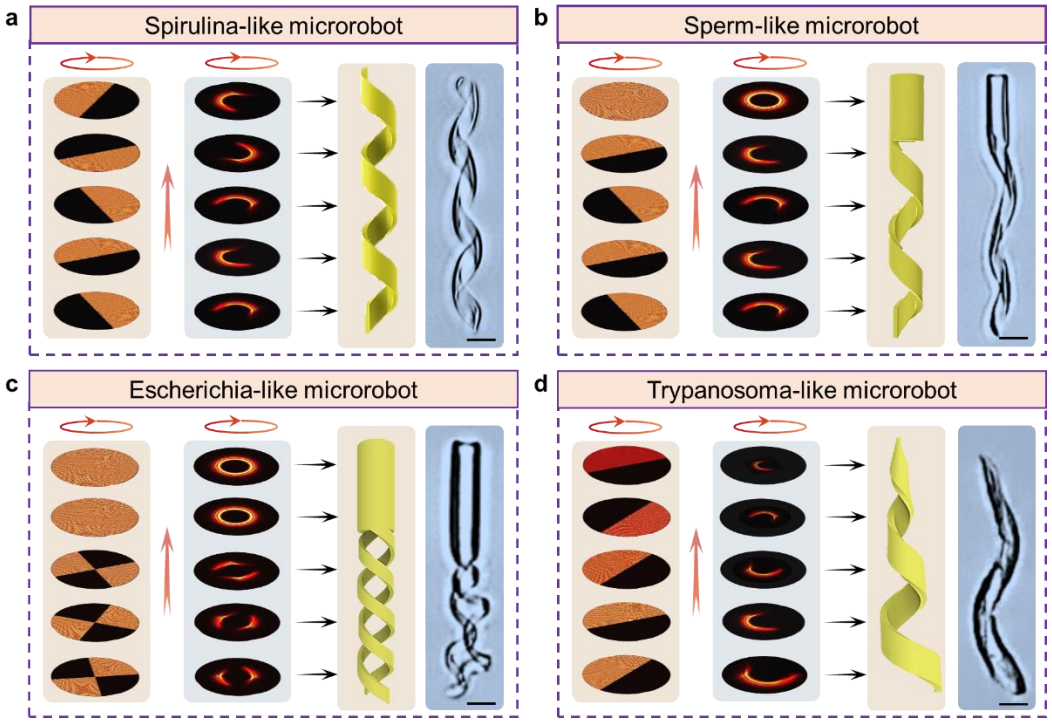

Figure S4. The high-efficient fabrication of polymorph biomimetic microhelices based on rotary holographic processing method. The fabrication of (a) Spirulina-like microhelix with cylindrical helical morphology, (b) Sperm-like microhelix with one head and one helical tail, (c) Escherichia-like microhelix with one head and two helical tails and (d) Trypanosoma-like microhelix with conical helical morphology. The first column is the RCGH; The second column is the RHRB; The third columns are the schematic diagram and optical image of contracted bionic helical microhelix. All scale bar: 10 μm.

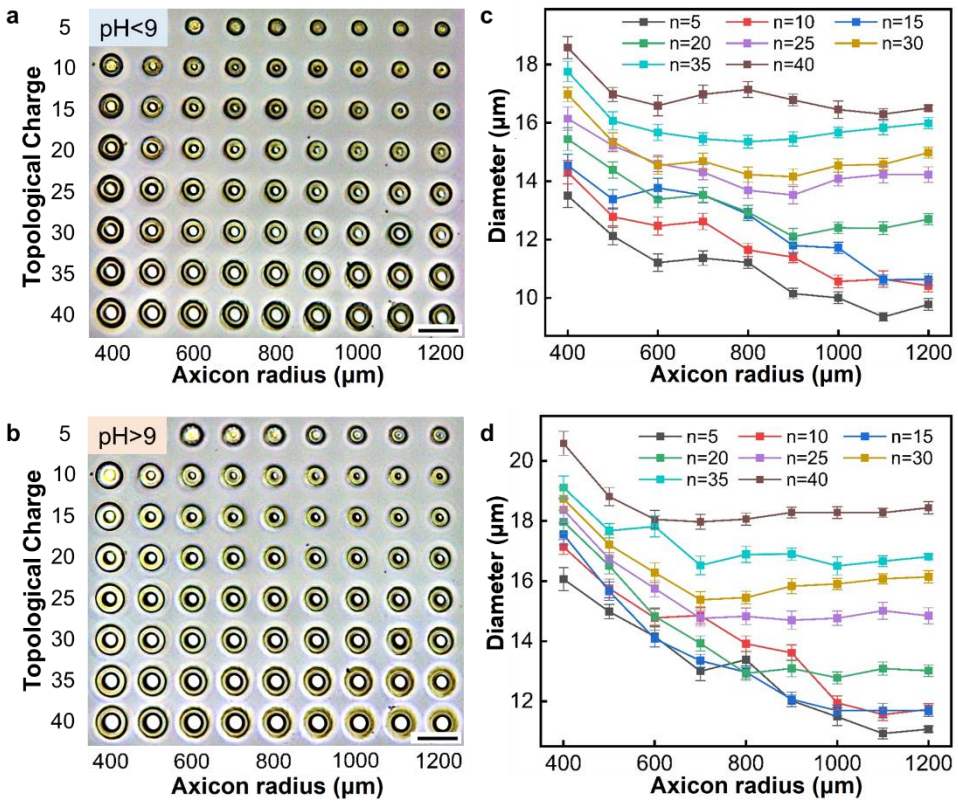

Figure S5. Dependence of the diameter of microrings in contracted (upper) and expanded (under) states on the axicon radius and topological charge of CGH. The optical images of hydrogel microrings in contracted state (a) and expanded state (b). The diameter of microrings as a function of axicon radius and topological charge of CGH in contracted state (c) and expanded state (d). All scale bar: 25 μm.

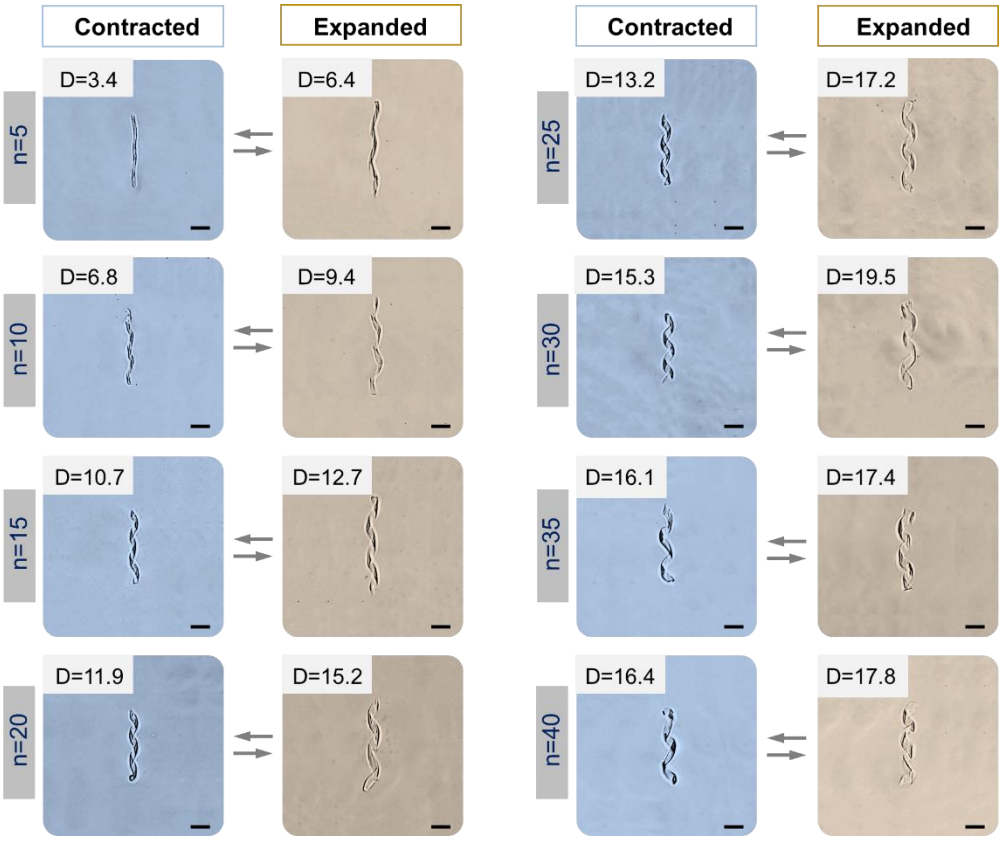

Figure S6. The optical images of contracted and expanded microhelixes with different diameters, controlled by the topological charge (*n*=5~40) of CGH. All scale bar: 25 μm.

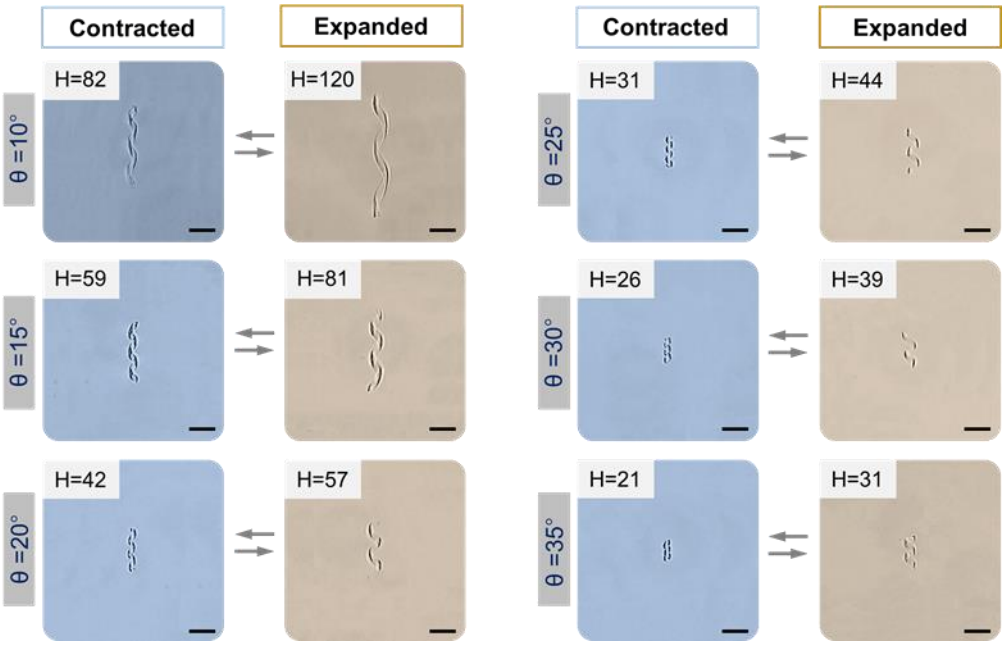

Figure S7. The optical images of contracted and expanded microhelixes with different heights, controlled by the rotating angle θ_0 (10~35°) of RHRB. All scale bar: 25 μm.

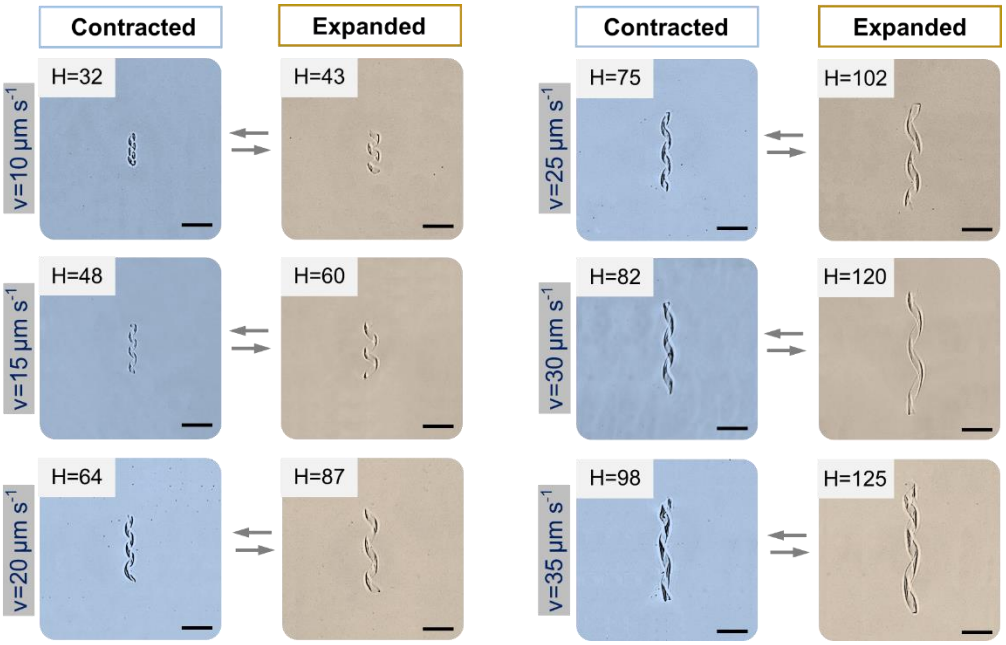

Figure S8. The optical images of contracted and expanded microhelixes with different heights, controlled by the scanning speed (V=10~35 μm s^{-1}) of sample stage. All scale bar: 25 μm.

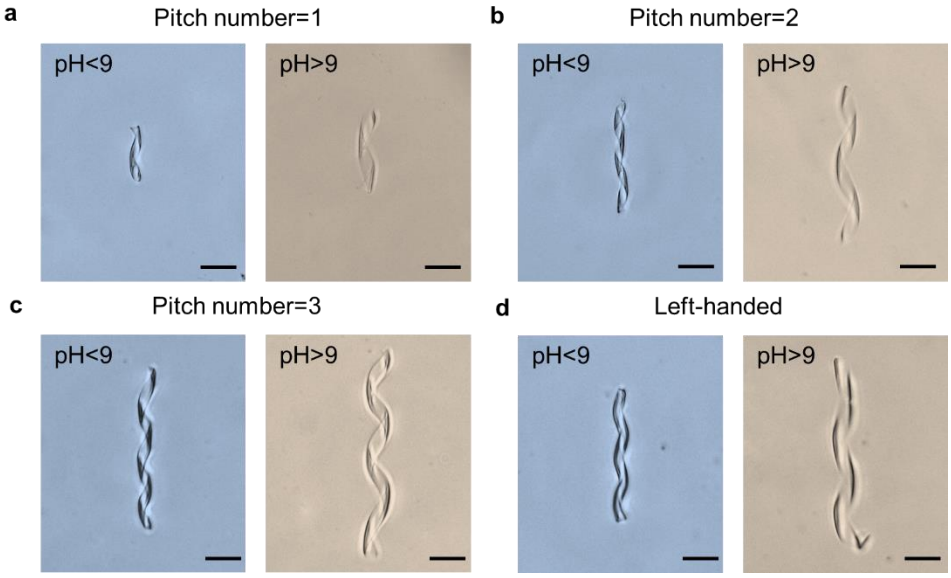

Figure S9. The optical images of contracted and expanded microhelixes with different pitch numbers (a-c) and helix senses (d). Scale bar: 25 μm.

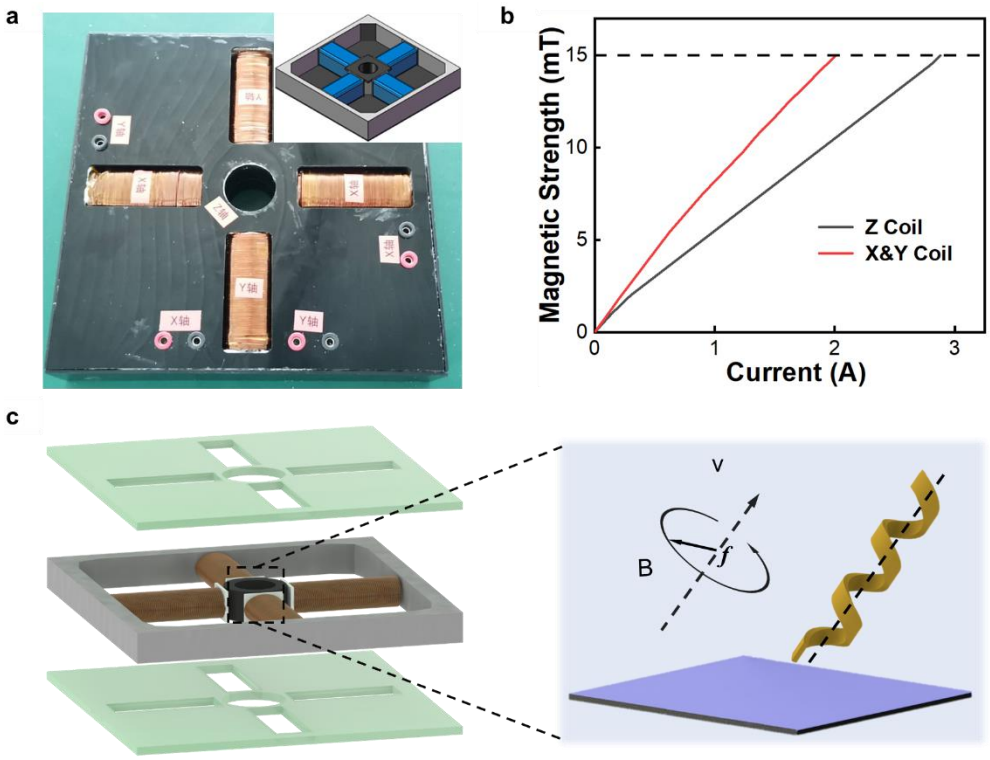

Figure S10. The magnetic actuation system. (a) The magnetic field generator to create a uniform 3D rotating magnetic field in the central region. (b) The strength of magnetic field in the x, y and z direction proportional to the input current. (c) Schematics of the magnetic actuation for helical microswimmer in 3D rotating magnetic field.

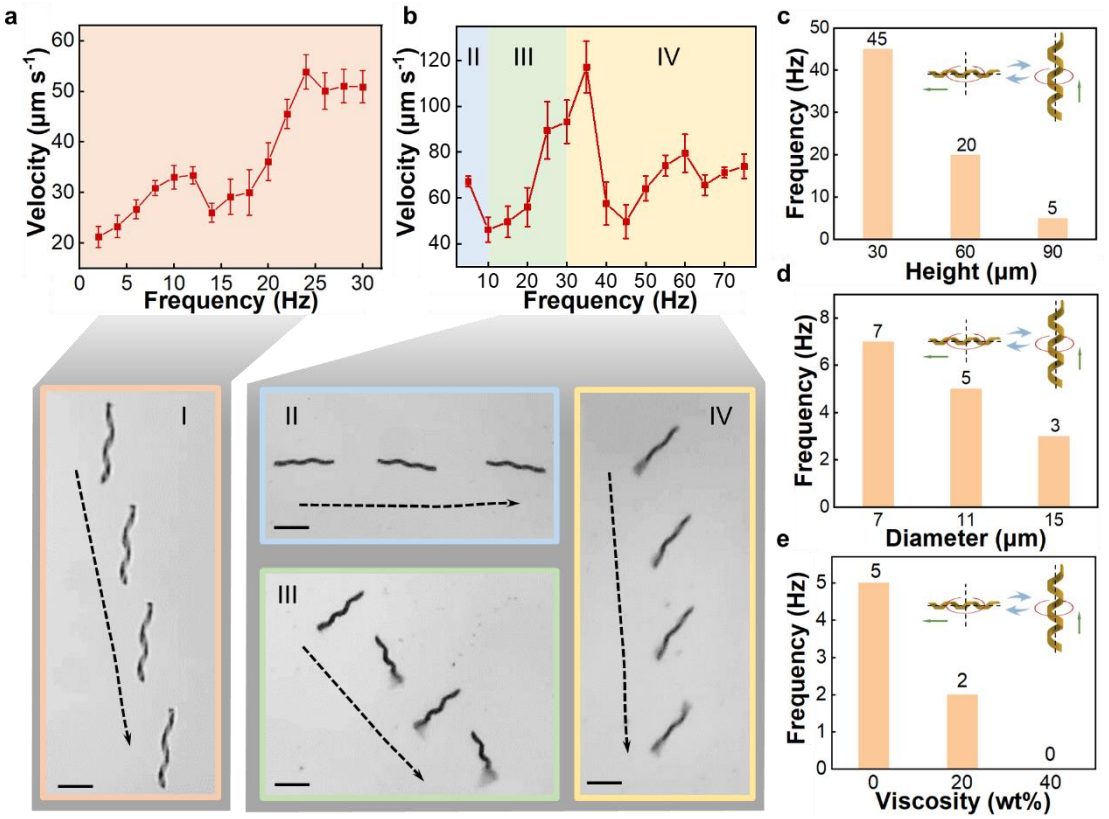

Figure S11. The magnetic actuation characteristics of helical microswimmer in contracted and expanded states. (a) The swimming speed of expanded helical microswimmer with respect to the input magnetic field frequency. As the frequency increases, the microswimmer keeps the corkscrewing motion (mode I). (b) The swimming speed and modes of contracted helical microswimmer versus the input magnetic field frequency. As the frequency increases, the microswimmer demonstrates three motion modes: II, tumbling (f < 10 Hz); III, wobbling (10 Hz < f < 30 Hz); IV, corkscrewing (f > 30 Hz). The transforming frequency of microswimmer's motion mode from II to I varying with the height (c) and diameter (d) of helical microswimmer and the viscosity of solution (e). All scale bar: 50 μm.

Note S1. The detailed description of the magnetic actuation characteristics of helical microswimmer

As shown in Figure S11a, the velocity of expanded helical microswimmer is not in direct proportion to the frequency before the step-out frequency (24 Hz). Besides, after the step-out frequency, the velocity doesn't drop sharply and remains relatively high as the frequency continuously increases. These are unique swimming behaviors compared with rigid helical microswimmers. According to the swimming

characterization of previously reported soft helical microswimmer,[1] these unique behaviors are most probably caused by the low storage modulus of hydrogel in expanded state, which is soft and prone to transforming when subjecting to strong magnetic torques.

Figure S11b reveals that the contracted microswimmer has three motion modes (tumbling, wobbling and corkscrewing) with the frequency increasing. There is a sharp drop after the frequency exceeding 35 Hz. This is primarily due to the enhanced storage modulus of contracted hydrogel microswimmer, which loses plenty of water in the dehydration process. However, as the increasing of frequency, the velocity of contracted microswimmer keeps relatively high, which shows the same tendency with expanded microswimmer due the same reason.

Although the motion mode of contracted microswimmer can be altered by changing the frequency, the steerabilities of microswimmer in mode III and mode IV are poor, which are not adopted in our experiment.

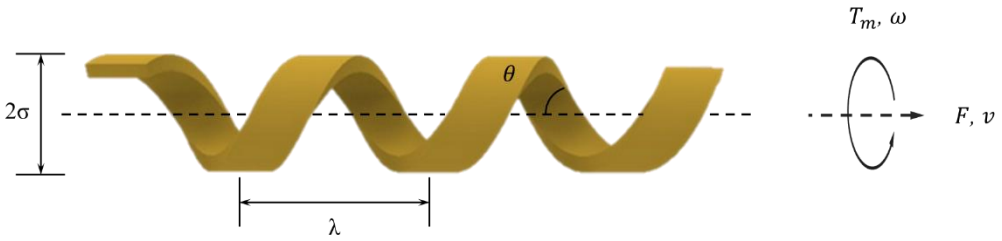

Figure S12. The geometrical parameters, and the stress and movement situation of magnetic helical microswimmer.

Note S2. The qualitative analysis of the transition between tumbling and corkscrewing motions

The magnetic propulsion of helical microswimmers at low Re number have received plenty of studies for several decades.[2-4] The linear relationship between the drag force $\boldsymbol{F_d}$, torques $\boldsymbol{T_d}$, the microswimmer's velocity $\boldsymbol{U}$ and rotational speed $\boldsymbol{\Omega}$ can be expressed as follow [5]

$$\begin{pmatrix} \boldsymbol{F_d} \\ \boldsymbol{T_d} \end{pmatrix} = -\begin{pmatrix} A & B \\ B^T & C \end{pmatrix}\begin{pmatrix} \boldsymbol{U} \\ \boldsymbol{\Omega} \end{pmatrix} \tag{1}$$

Where A, B and C are 3×3 matrices and are functions of the microswimmer's geometry and fluid viscosity only.

The equation (1) can be simplified by considering only the rotation around and the translation along the helical axis (Figure S12). This results in a simple 2×2 resistant matrix with scalar entries a, b and c.[6] Furthermore, the external force is assumed to be zero because the helix moves in a horizontal, unobstructed plane, and without the application of magnetic gradient forces.

$$\begin{pmatrix} 0 \\ T_m \end{pmatrix} = -\begin{pmatrix} a & b \\ b & c \end{pmatrix}\begin{pmatrix} v \\ w \end{pmatrix} \tag{2}$$

The T_m in equation (2) is equal to T_d in equation (1) due to the moment equilibrium. The three parameters a, b and c are expressed as [7]

$$a = 2\pi n\sigma\left(\frac{\xi_{\parallel}cos^2\theta + \xi_{\perp}sin^2\theta}{sin\theta}\right) \tag{3}$$

$$b = 2\pi n\sigma^3\left(\frac{\xi_{\perp}cos^2\theta + \xi_{\parallel}sin^2\theta}{sin\theta}\right) \tag{4}$$

$$c = 2\pi n\sigma^3\left(\frac{\xi_\perp cos^2\theta + \xi_\parallel sin^2\theta}{sin\theta}\right) \quad (5)$$

where the $\xi_\perp$ and $\xi_\parallel$ are the resistance coefficients perpendicular to the filament and along the filament. n denotes the pitch number. σ and r represent the radius and line radius of microswimmer. θ means the helical angle.

According to the simplified resistive force theory (RFT) established by Grey and Hancock,[8] the RFT divides the drag force on a helical filament into the force components along and perpendicular to the filament and relates these forces to the local velocities $v_\perp$ and $v_\parallel$. On an infinitesimally small length of filament, the parallel and perpendicular forces are

$$dF_n = \xi_\perp v_\perp ds \quad (6)$$

$$dF_s = \xi_\parallel v_\parallel ds \quad (7)$$

And the drag coefficients are given by[9]

$$\xi_\perp = \frac{4\pi\eta}{\ln\left(\frac{0.36\sigma}{rsin\theta}\right) + 0.5} \quad (8)$$

$$\xi_\parallel = \frac{2\pi\eta}{\ln\left(\frac{0.36\sigma}{rsin\theta}\right)} \quad (9)$$

where the η indicates the dynamic viscosity of liquid.

As is well known, at low frequency of the rotating magnetic field the helical microswimmer tumbles in the plane of the field rotation at low frequency of the rotating magnetic field. Upon increasing the field frequency, the tumbling switches to wobbling and the precession angle (β, between the axis of the field rotation and the helical axis) gradually diminishes resulting in a corkscrewing motion. To explain this, Alexander *et al* studied in detail the dynamics of ferromagnetic chiral microswimmers and established the relationship between their orientation and propulsion with the actuation frequency, remanent magnetization and the geometry.[10] The transition frequency (w_t) of microswimmer from tumbling to wobbling can be expressed as

$$\omega_t = \frac{m \times H_e}{c} \quad (10)$$

where m stands for the magnetization intensity of microswimmer and the H_e denotes the amplitude of external rotating magnetic field. The c is the parameter in equation (5). Substituting the equation (5) into equation (10) yields the following equation

$$\omega_t = \frac{m \times H_e}{2\pi n\sigma^3 \left(\frac{\xi_\perp cos^2\theta + \xi_\parallel sin^2\theta}{sin\theta}\right)} \tag{11}$$

For the swelling process of our hydrogel helical microswimmer, the major changing is the structure parameters such as the radius σ, the height H and the line radius r. The magnetization intensity m may have negligible changes because there are little Fe_3O_4 nanoparticles falling off from the hydrogel microswimmer during the expansion process. Besides, the H_e keeps constant during the while process. Therefore, from equation (8), (9) and (11), we can conclude that the radius σ has a major effect on the transition frequency (w_t) due to the w_t nearly inversely proportional to the σ^3. This can explain why our hydrogel microswimmer shows tumbling motion in contracted state and corkscrewing motion in expanded state. The contracted microswimmer has a smaller w_t owing to a smaller radius σ while the expanded microswimmer has a larger w_t because of a larger radius σ. The actuation frequency 5 Hz is less than the w_t of contracted microswimmer but is greater that the w_t of expanded microswimmer. What's more, the experimental results of w_t changing with the height and diameter of helical microswimmers and the viscosity of liquid in Figure S11c-e can firmly verify the equation (11).

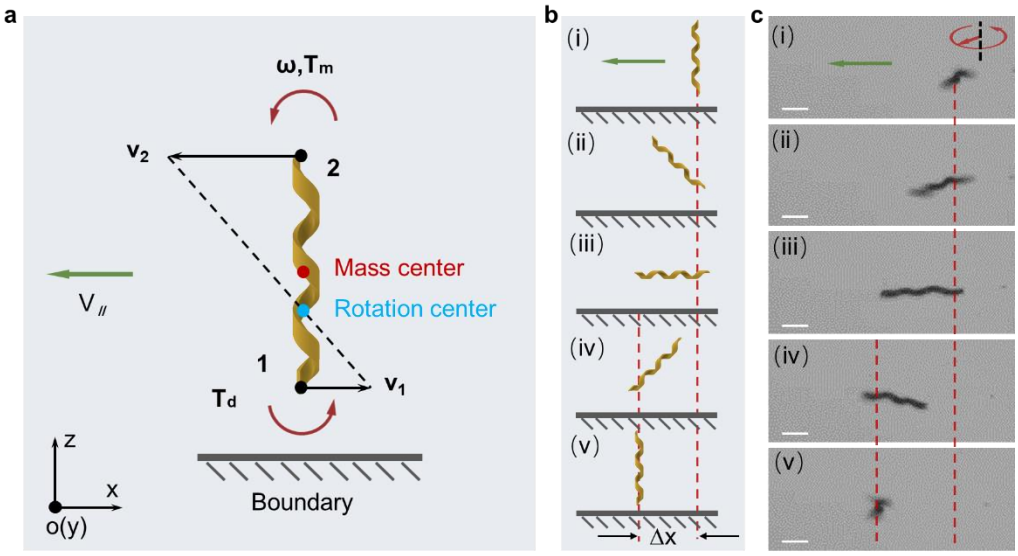

Figure S13. Mechanism analysis of the tumbling motion of contracted helical microswimmer. (a) Schematic showing that the velocities at two ends of the contracted helical microswimmer are different, due to inhomogeneous boundary conditions. (b) Schematic diagram of the tumbling process of contracted helical microswimmer during half cycle. (c) The optical images of contracted helical microswimmer at different moments, corresponding to (b). Scale bar: 25 μm.

Note S3. Mechanism analysis of contracted microswimmer's tumbling forward

As shown in Figure S13, the contracted microswimmer tumbles with a constant angular velocity ω. It is well known that the drag efficient of an object increases when it approaches a boundary.[11-13] Therefore, the hydrodynamic interaction of the microswimmer with the boundary is stronger on the '1' end than that on the '2' end, resulting in a velocity difference between the two ends of the microswimmer, i.e., $v_1 < v_2$. The velocity difference will remain unaltered until the long axis of the microswimmer parallel to the boundary when the boundary conditions of the microswimmer's two ends are symmetric. During this time, the mass center is above the rotation center and rotates around the rotation center to the left. Then the '2' end is lower than '1' end and $v_2 < v_1$, but the mass center is still above the rotation center and rotates around the rotation center to the left. This simplified model explains why a tumbling microswimmer can move forward near the boundary. Besides, we can conclude that the velocity of tumbling microswimmer is increasing with the growing of the height of microswimmer, which is in accord with the data in Figure 3f.

Table S1 The velocities of microswimmer with different heights and diameters in contracted and expanded states

Velocity ($\mu m\ s^{-1}$)	Different height			Different diameter		
	H=30 μm	H=60 μm	H=90 μm	D=7 μm	D=11 μm	D=15 μm
pH<9	43.5	56	67.13	64.49	67.13	65.49
pH>9	9.27	33.58	25.02	19.46	25.02	37.04
Times	4.69	1.67	2.68	3.42	2.68	1.75

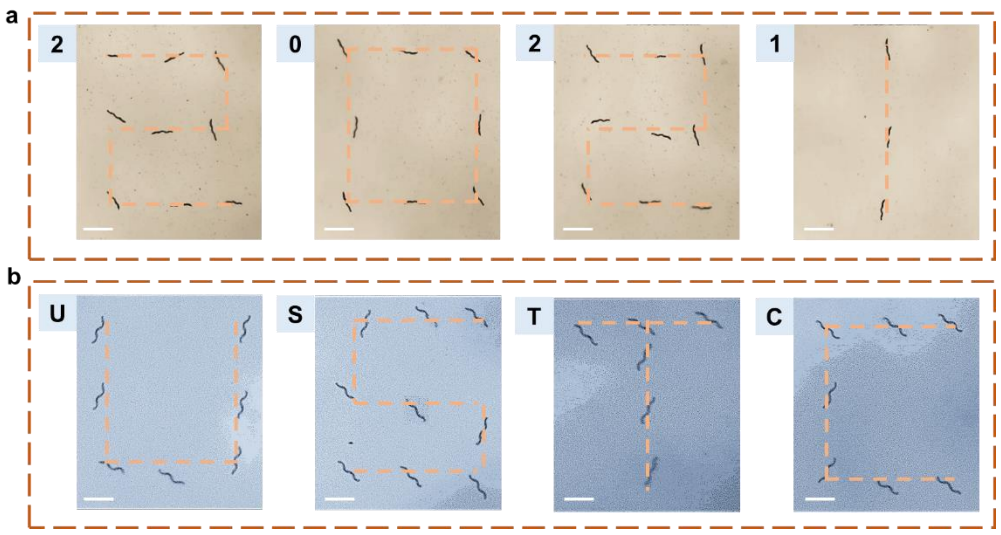

Figure S14. Stimuli-responsive helical microswimmer is steered by external magnetic field to swim along different patterns in contracted and expanded states. (a) In the contracted state, the helical microswimmer is steered to swim along "2" "0" "2" "1" tracks. (b) In the expanded state, the helical microswimmer is steered to swim along "U" "S" "T" "C" patterns. Throughout this process, the external magnetic field only changes the direction. All scale bar: 120 μm.

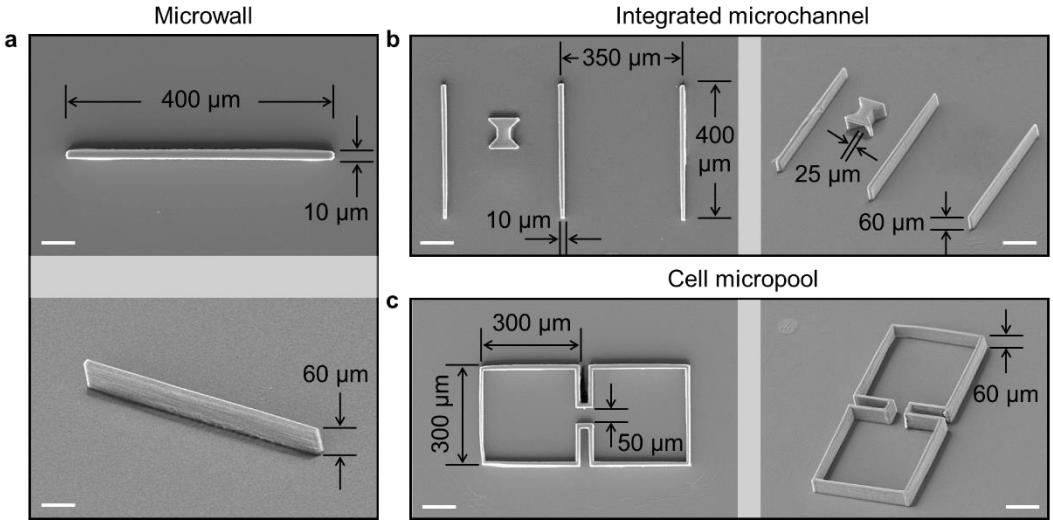

Figure S15. The sizes of microwall, integrated microchannel and cell micropool fabricated by fs-DLW. (a) The microwall with the length of 400 μm, the width of 10 μm and the height of 60 μm. Scale bar: 50 μm. (b) The integrated microchannel consisting of two channels and a microtunnel. The channel is formed by two microwalls with the length of 400 μm, the width of 10 μm and the height of 60 μm. The distance between two microwalls is 350 μm. The width of the internal microtunnel is 50 μm. (c) The cell micropool composed of two square pools and a microchannel. The square pool is surrounded microwall with the length of 300 μm, the width of 10 μm and the height of 60 μm. The width of the internal microchannel is 50 μm. The scale bars in (b) and (c) are 100 μm.

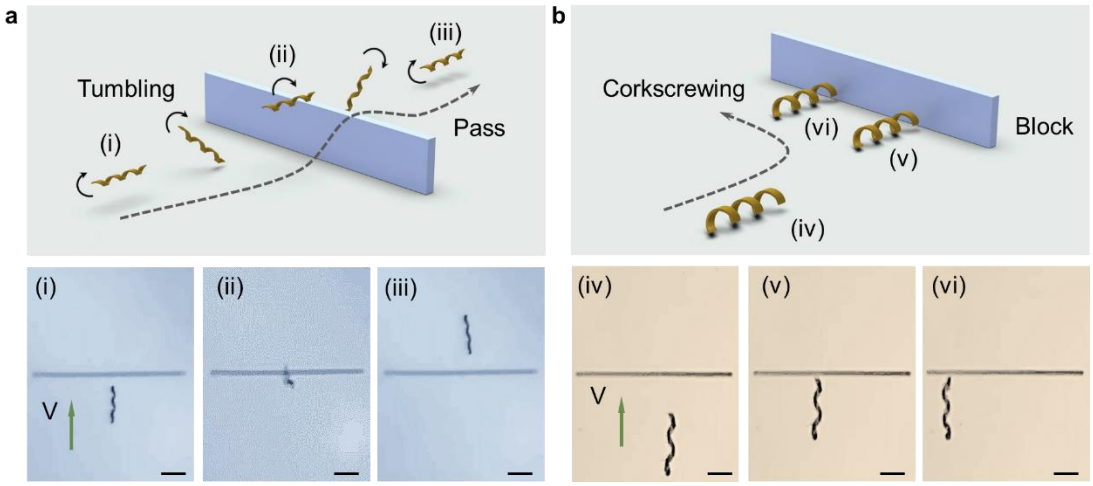

Figure S16. Schematics of microswimmer crossing microwall. (a) The schematic diagram and optical images of contracted microswimmer tumbling across the microwall. (b) The schematic diagram and optical images of expanded microswimmer tumbling but blocked by the microwall. Scale bar: 50 μm.

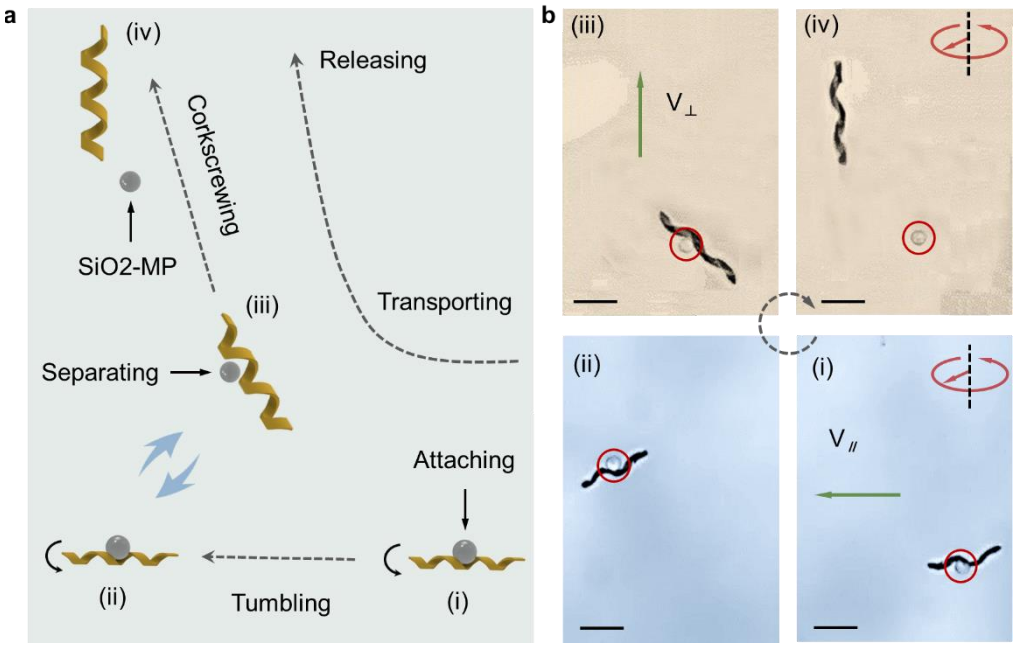

Figure S17. The transportation and release of SiO_2 microparticle (MP). (a) Schematic diagram of the contracted helical microswimmer transporting SiO_2 MP and expanded helical microswimmer releasing the SiO_2 MP. When the pH value is inferior to 9 and the hydrogel shrinks, experimental results show that the microswimmer has strong adhesion with SiO_2 MP and can tumble forward carrying the SiO_2 MP. On the contrary, when the pH value exceeding 9 and the hydrogel swelling, the SiO_2 MP is released due to the adhesiveness between SiO_2 MP and microswimmer becoming weak. We assume that this phenomenon is due to the hydrogen bond between the hydrogel and the SiO_2 MP becoming weaker in alkaline solution (pH>9). The diameter of SiO_2 MP is 20 μm. (b) Optical images of the transportation and release of SiO_2 MP at different moments, corresponding to (a). Scale bar: 50 μm.

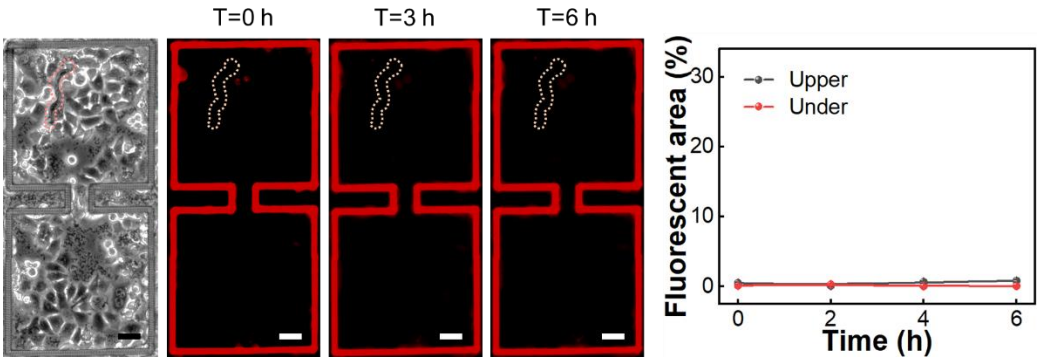

Figure S18. The control experiment of microswimmer without drugs at target position. After the same culturing time, there is no obvious red fluorescence in the upper and under micropools. Scale bar: 50 μm.

Supplementary movies:

Movie S1. Rotary holographic processing strategy to fabricate microhelices.

Movie S2. The shrinking and swelling process of microhelices.

Movie S3. Tumbling and corkscrewing motions of microrobot.

Movie S4. Tumbling-to-corkscrewing transition of microswimmer.

Movie S5. Passing microwall.

Movie S6. Passing integrated microchannels.

Movie S7. Transporting cargo.

References

[1] X. Wang, X. H. Qin, C. Hu, A. Terzopoulou, X. Z. Chen, T. Y. Huang, K. Maniura-Weber, S. Pané, B. J. Nelson, *Adv. Funct. Mater.* **2018**, *28*, 1804107.

[2] A. M. Leshansky, K. I. Morozov, B. Y. Rubinstein, *Nanoscale* **2016**, *8*, 14127-14138.

[3] K. I. Morozov, Y. Mirzae, O. Kenneth, A. M. Leshansky, *Phys. Rev. Fluids* **2017**, *2*, 044202.

[4] K. E. Peyer, L. Zhang, B. J. Nelson, *Nanoscale*, **2013**, *5*, 1259-1272.

[5] E. M. Purcell, *Am. J. Phys*. **1977**, *45*, 3-11.

[6] E. M. Purcell, *P. Natl. Acad. Sci. USA* **1997**, *94*, 11307-11311.

[7] J. J. Abbott, K. E. Peyer, M. C. Lagomarsino, L. Zhang, L. Dong, I. K. Kaliakatsos, B. J. Nelson, *Int. J. Rob. Res.* **2009**, *28*, 1434–1447

[8] J. Gray, G. Hancock, *J. Exp. Biol.* **1955**, *32*, 802-814.

[9] J. Lighthill, *SIAM Rev.* **1976**, *18*, 161-230.

[10] K. I. Morozov, A. M. Leshansky, *Nanoscale* **2014**, *6*, 12142-12150.

[11] N. D. Mestre, W. Russel, *J. Eng. Math.* **1975**, *9*, 81-91.

[12] E. Lauga, T. R. Powers, *Rep. Prog. Phys.* **2009**, *72*, 096601.

[13] L. Zhang, T. Petit, Y. Lu, B. E. Kratochvil, K. E. Peyer, R. Pei, J. Lou, B. J. Nelson, *ACS Nano* **2010**, *4*, 6228-6234.